mater.scichina.com link.springer.com

Published online 9 April 2021 | https://doi.org/10.1007/s40843-020-1622-8
Sci China Mater 2021, 64(9): 2230–2241

Rich oxygen vacancies mediated bismuth oxysulfide crystals towards photocatalytic CO_2-to-CH_4 conversion

Lisha Jiang[1], Yuan Li[1], Xiaoyong Wu[1] and Gaoke Zhang[1,2,3*]

ABSTRACT **Oxygen vacancy-rich bismuth oxysulfide (Bi_2O_2S) with layered structure was prepared for efficient photocatalytic CO_2 reduction under visible light irradiation. The existence of rich oxygen vacancies in Bi_2O_2S, which was proven by sufficient characterization, can provide abundant active sites, improve CO_2 adsorption and activation abilities and boost the separation efficiency of photogenerated carriers, as determined by theoretical and experimental analyses. As a result, Bi_2O_2S with rich oxygen vacancies achieves excellent CO_2 conversion with a CH_4 production of 65.8 μmol g^{-1} under 90 min of visible light irradiation, which was 27-fold higher than the pristine Bi_2O_2S. The mechanism of photocatalytic conversion of CO_2 to CH_4 was also determined by *in situ* FT-IR analyses. This study provides an in-depth understanding of the development of Bi-O-S system photocatalysts through defect engineering for photocatalytic CO_2 reduction.**

Keywords: oxygen vacancies, bismuth oxysulfide, charge separation, photocatalysis, CO_2 reduction

INTRODUCTION

The energy crisis and environmental pollution have been challenges worldwide. Solar energy, as a promising style of clean energy, has attracted a considerable amount of interest [1,2]. Converting CO_2 into value-added fuels, including CH_4, in the presence of solar energy can efficiently reduce environmental pollution and alleviate the energy crisis [3,4]. However, the photocatalytic CO_2 reduction performance is still limited by the low separation and transfer efficiencies of photogenerated carriers and the poor stability of the photocatalyst. In recent decades, much attention has been paid to the fabrication of multiple photocatalysts with special properties, but their properties are still vital factors in the photocatalytic CO_2 reduction process. To enhance the photocatalytic CO_2 reduction performance, facilitating the separation of photogenerated carriers and constructing active sites to boost the activation of CO_2 by the photocatalysts are desirable approaches.

Layered materials have been explored widely for photocatalytic reactions due to their unique and excellent photoelectric properties [5,6]. The unique layered structure with a built-in electrostatic field enables BiOX (X = Cl, Br, I), which is typical bismuth-based layered material, to be an efficient photocatalyst with enhanced photogenerated carrier separation efficiency [7–11]. In the crystal structure of BiOX, $[Bi_2O_2]^{2+}$ slabs are interleaved with double slabs of halogen atoms, which can be held in place by electrovalent bonds along the [001] direction [12], thus endowing BiOX with excellent activity in photocatalytic reactions [13–15]; for example, defect-engineered BiOBr atomic layers are used for efficient visible-light-driven CO_2 reduction [14]. Bi_2O_2S (denoted as BiOS) is a new type of $[Bi_2O_2]^{2+}$-containing material whose crystal structure is similar to that of BiOX [16]. In the typical structure of BiOS, one column of S^{2-} anions separates the two $[Bi_2O_2]^{2+}$ layers. The different structures of BiOS and BiOX imply different charge properties [17]. The band gap of BiOS can be narrowed by S atoms between $[Bi_2O_2]^{2+}$ layers, allowing BiOS to maintain its excellent stability during photocatalytic reactions. Additionally, BiOS is usually used for solar cells because of its fast photoelectric response under light irradiation, efficient charge dissociation and transfer and long carrier

[1] State Key Laboratory of Silicate Materials for Architectures, Hubei Key Laboratory of Mineral Resources Processing and Environment, Wuhan University of Technology, Wuhan 430070, China
[2] Shenzhen Research Institute of Wuhan University of Technology, Shenzhen 518000, China
[3] Henan Institute of Advanced Technology, Zhengzhou University, Zhengzhou 450052, China
* Corresponding author (email: gkzhang@whut.edu.cn)

lifetime [18–20]. However, only a few studies focused on BiOS for photocatalytic reactions, including the transformation of Bi_2O_2S into superconducting $Bi_4O_4S_3$ [17], modified Bi_2O_2S/In_2O_3 composites and Bi_2WO_6-Bi_2O_2S 2D-2D heterojunctions for water splitting [21,22]. The structural and photoelectronic properties of BiOS have not yet been explored in detail.

The intrinsic electronic properties of materials have a considerable effect on electronic separation and transfer and thereby affect the photocatalytic performance of the materials [23]. A series of strategies have been adopted to tailor the electronic properties of materials, such as surface modification and functionalization, element doping, defect and phase engineering [24–27]. In particular, defect or vacancy control is a promising strategy to modify the electronic structure of photocatalysts. Vacancies are common defects observed in many materials, and have a crucial effect on the physicochemical properties of materials. It has been confirmed that oxygen vacancies can capture photogenerated electrons, promote the separation of photogenerated carriers and efficiently suppress the recombination of photogenerated electrons and holes. Additionally, the presence of oxygen vacancies can prolong the light absorption of the materials. Rich oxygen vacancies possess abundant localized electrons, which can enable them to serve as trapping centers to efficiently promote the capture and activation of the insert gases, including O_2, CO_2 and N_2 [28]. According to previous reports, the main defects in BiOX are oxygen vacancies because of the low bond energy and long bond length of the Bi–O bond. The presence of oxygen vacancies in BiOX can contribute to improving its photocatalytic performance [29]; for example, oxygen vacancies induced flexible BiOCl to exhibit superb photocatalytic CO_2 reduction activity [13]. However, no report has investigated the photocatalytic CO_2 reduction process of BiOS, another new $[Bi_2O_2]^{2+}$-containing material with rich oxygen vacancies.

In this work, the $[Bi_2O_2]^{2+}$-containing material BiOS with rich oxygen vacancies (BiOS-OV) was prepared through a thermal treatment method under different reaction conditions. The optimized BiOS-OV material revealed outstanding photocatalytic CO_2 reduction activity under visible light irradiation. The electronic structure was engineered by rich oxygen vacancies, resulting in the formation of new defect level. The enhanced photocatalytic CO_2 reduction activity was ascribed to the formed abundant active sites, which lead to excellent CO_2 adsorption and activation abilities and facilitate the separation of photogenerated carriers over the photocatalysts. The vital effect of the rich oxygen vacancies on the enhanced photocatalytic CO_2 reduction performance was confirmed through both theoretical calculations and experimental analyses. Furthermore, the mechanism of photocatalytic CO_2 reduction was also explored by *in situ* FT-IR analyses. This work provides an efficient strategy to improve the photocatalytic performance of $[Bi_2O_2]^{2+}$-containing materials through defect engineering.

EXPERIMENTAL SECTION

Preparation of photocatalysts

Bi_2O_2S was synthesized through a hydrothermal method. In detail, 1.9403 g of $Bi(NO_3)_3{\cdot}5H_2O$ and 0.1522 g of $SC(NH_2)_2$ were added to 60 mL of distilled water with continuous stirring and then 12 g of $LiOH{\cdot}H_2O$ was added to the above mixture to prepare a homogeneous solution. The mixture was transferred in an 80-mL stainless steel PPL-line autoclave and heated for three days at 200°C. After the autoclave was cooled to room temperature, the samples were washed with distilled water and then dried at 60°C. The collected sample was denoted as BiOS. Bi_2O_2S with rich oxygen vacancies was prepared through a thermal treatment method under a N_2 atmosphere at different temperatures for 2 h (denoted as BiOS-temperature) and at 400°C for different times (denoted as BiOS-time). In particular, the defective BiOS prepared under the optimized conditions of heating at 400°C for 4 h was denoted as BiOS-OV.

Characterization

X-ray diffraction (XRD) patterns were collected with a D/MAX-RB (Japan) diffractometer with Cu Kα radiation. The morphologies of the as-prepared photocatalysts were observed by field emission scanning electron microscopy (FESEM). The structural properties were further characterized *via* transmission electron microscopy (TEM, Talos F200S, Thermo Fisher, America). The X-photoelectron spectroscopy (XPS) was collected on a Thermo ESCALAB 250XI (America), and diffuse reflectance spectra (DRS) were obtained *via* a UV-Vis-NIR spectrophotometer (Shimadzu UV-3600 Plus, Japan). Photoluminescence (PL) emission spectra were collected on an RF-5301PC spectrofluorometer (Shimadzu, Japan). The time-resolved photoluminescence emission spectra were recorded with an excitation wavelength of 260 nm (Edinburgh Instruments, FLSP-920). Electron paramagnetic resonance (EPR) signals were collected on a Bruker instrument (A-300). CO_2 adsorption isotherms were obtained on a Micromeritics ASAP 2020, and CO_2

temperature-programmed desorption (TPD) spectra were collected on a catalyst analyzer (AutoChem II 2920).

Photocatalytic CO_2 reduction reaction

The activities of the as-prepared photocatalysts were measured *via* a photocatalytic CO_2 reduction reaction in a 200-mL reactor (Perfectlight, China). Typically, 30 mg of the as-prepared sample was dispersed on a 5-cm diameter container *via* ultrasonic treatment, where the sample was placed in the top of the reactor, while 1.2 g of Na_2CO_3 was added into the bottom of this reactor. Before light irradiation (300 W of Xe lamp with a 420-nm filter), N_2 was employed to remove air from the reactor, and vacuum treatment was then applied. After that, 2 mL of H_2SO_4 (1:1 vol.) was injected into the reactor to generate CO_2 gas. The products of photocatalytic CO_2 reduction were analyzed *via* gas chromatography (GC, GC-7820, Zhongkehuifen China).

Photoelectrochemical measurement

A CHI660E station with a three-electrode system was used to test the transient photocurrent response and electrochemical impedance spectroscopy (EIS) curves by using a 0.5 mol L^{-1} Na_2SO_4 solution as the electrolyte. Platinum wire and Ag/AgCl electrodes counter electrodes were used as the counter electrode and reference electrode, respectively. The as-prepared sample films on fluorine-doped stannic oxide glass were used as working electrodes.

Theoretical calculation

Density functional theory (DFT) calculations were performed by the Vienna *Ab-Initio* Simulation Package (VASP) with the PerdewBurke-Ernzerh (PBE) functional and the Generalized Gradient Approximation (GGA), in which the plane-wave cutoff energy was 400 eV, the energy converged to 10^{-5} eV/atom and the force converged was 0.02 eV/Å.

RESULTS AND DISCUSSION

A series of BiOS samples with oxygen vacancies were synthesized to optimize the thermal treatment process. As shown in Fig. 1a and b, all the as-prepared BiOS samples with oxygen vacancies were well indexed with the standard orthorhombic Bi_2O_2S structure (PDF No. 34-1493). Fig. 1c also shows the XRD patterns of BiOS-OV and

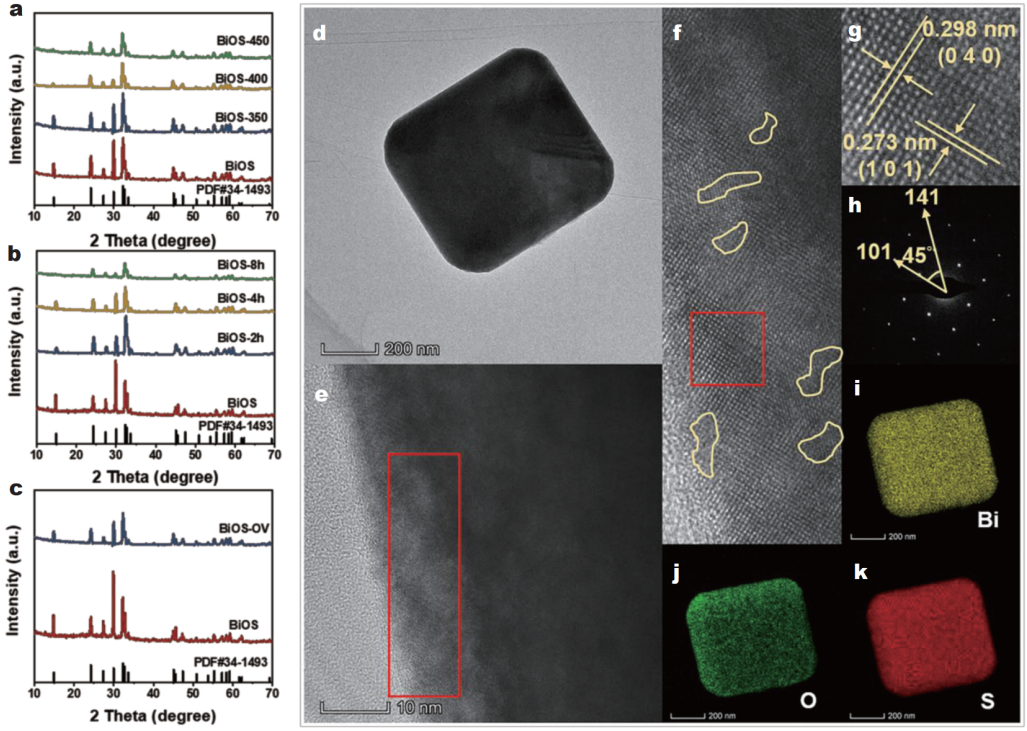

Figure 1 XRD patterns of the as-prepared samples under different heating conditions: (a) different heating temperatures and (b) different heating times. (c) XRD patterns of the pristine BiOS and BiOS-OV prepared under the optimized treatment conditions. (d) TEM image of the BiOS-OV. (e) HRTEM image of BiOS-OV; (f) and (g) enlarged HRTEM images. (h) SAED pattern of the BiOS-OV. Elemental mapping images of BiOS-OV: (i) Bi, (j) O and (k) S.

pristine BiOS. No other peaks were observed in the XRD patterns, precluding the existence of other phases in BiOS-OV after the heating treatment. The morphologies and microstructures of the photocatalysts were observed through FESEM. As exhibited in Fig. S1, the pristine BiOS exhibits a brick-like morphology. After thermal treatment, the BiOS-OV still maintains the same morphology as the pristine BiOS, indicating that the heating treatment has no significant effect on the morphologies of the BiOS samples with oxygen vacancies. The morphology and microstructure of BiOS-OV were further observed *via* TEM. As seen in Fig. 1d, a regular brick-like surface is in the TEM image of BiOS-OV. The HRTEM image of the pristine BiOS (Fig. S2) revealed clear crystalline structure. However, a few regions of disordered structures were observed in the HRTEM images of BiOS-OV (Fig. 1e and f), indicating that BiOS-OV possesses more defects than the pristine BiOS [15]. Additionally, BiOS-OV exhibits obvious lattice fringes, in which interplanar spacings of 0.298 and 0.273 nm were observed (Fig. 1g), consistent with the XRD analyses. As shown in Fig. 1h, the corresponding selected area electron diffraction (SAED) pattern reveals the single-crystalline property of the as-prepared BiOS-OV sample. The angle of adjacent spots marked in the SAED pattern was 45°, which is assigned to the theoretical value of the angle between the (141) and (101) planes of orthorhombic Bi_2O_2S. Therefore, the [$\bar{1}$01] zone axis of the BiOS-OV was obtained based on the above analyses. Moreover, the elemental mapping images (Fig. 1i–k) show the uniform distribution of Bi, O and S elements overlapped along the whole brick-like structure, indicating the successful synthesis of BiOS-OV.

The chemical compositions of the pristine BiOS and BiOS-OV were analyzed by XPS analyses. As shown in Fig. S3, Bi, O and S were all observed in the XPS spectra of BiOS and BiOS-OV, revealing the high purity of the photocatalysts. The Bi $4f_{7/2}$ and Bi $4f_{5/2}$ peaks of the pristine BiOS located at 158.7 and 164.0 eV with a peak split of 5.3 eV are assigned to Bi^{3+} (Fig. 2a) [17]. Compared with those of the pristine BiOS, the Bi 4f peaks in the spectrum of BiOS-OV shift to lower binding energies, which can be ascribed to cleavage of the Bi–O bond

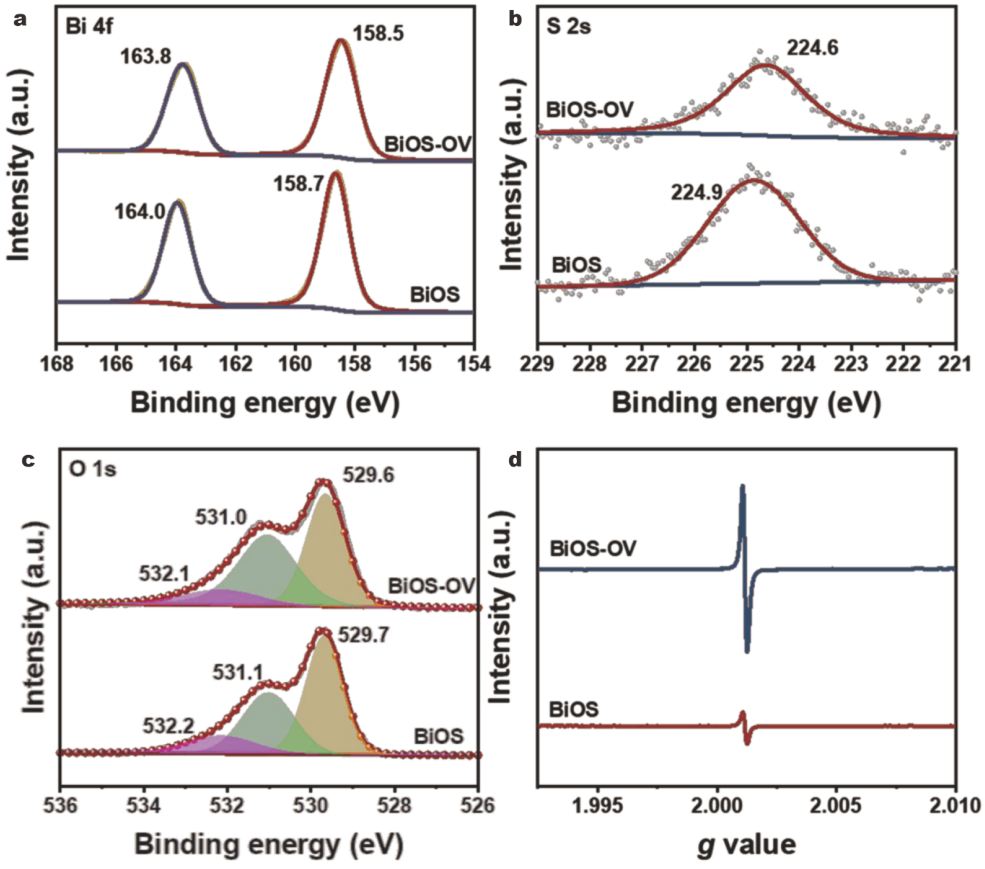

Figure 2 XPS spectra of pristine BiOS and BiOS-OV: (a) Bi 4f, (b) S 2s and (c) O 1s. (d) EPR spectra of the BiOS and BiOS-OV samples.

caused by the presence of oxygen vacancies [14,30,31]. Furthermore, the peak centered at 224.9 eV corresponds to S 2s, confirming the presence of S in BiOS (Fig. 2b) [17]. The S 2s peak in the XPS spectrum of BiOS-OV also exhibits an obvious shift. As illustrated in the O 1s XPS spectrum of BiOS, three peaks were observed (Fig. 2c). The peak located at 529.7 eV (marked as O_α) corresponds to the Bi–O bond of BiOS, while the peak at 532.2 eV corresponds to the adsorbed water (marked as O_γ). Additionally, the peak at a binding energy of 531.1 eV is ascribed to the surface adsorbed oxygen (marked as O_β), such as O_2^-, O^- (oxygen vacancies) and hydroxyl-like groups [32,33]. It is obvious that the peak centered at 531.0 eV from the XPS spectrum of BiOS-OV is stronger than that in pristine BiOS because of the contribution of rich oxygen vacancies in BiOS-OV [34]. Furthermore, the O 1s peaks in the spectrum of BiOS-OV also shift to lower energies. The area ratio of Bi–O in BiOS-OV (45.1%) is smaller than that of pristine BiOS (52.3%), while the oxygen vacancies in BiOS-OV show an increased area ratio (44.5%) in contrast to those in pristine BiOS (35.2%). As exhibited in Table S1, the O_β/O_α value of BiOS-OV is higher than that of BiOS, revealing an increase in surface oxygen vacancies [32]. The enhanced oxygen vacancy concentration in BiOS-OV is ascribed to the reduction of oxygen atoms connected to Bi atoms in BiOS-OV [12]. To further confirm the properties of the oxygen vacancies, EPR characterization was also employed. As depicted in Fig. 2d, a stronger EPR signal attributed to the oxygen vacancies was observed at g = 2.002 in BiOS-OV than in pristine BiOS [34]. The XPS and EPR results further confirm the presence of introduced rich oxygen vacancies in BiOS-OV.

The optical properties of the photocatalysts were explored *via* DRS. Fig. S4 shows the DRS spectra of the BiOS and BiOS samples with oxygen vacancies under different heating conditions. The absorption spectra of all the as-prepared BiOS samples with oxygen vacancies exhibit a slight redshift compared with that of pristine BiOS, indicating that the existence of rich oxygen vacancies had a substantial effect on the optical properties [15,35]. In particular, the DRS spectra of pristine BiOS and BiOS-OV are shown in Fig. 3a. Their corresponding $(\alpha h\nu)^{1/2}$ *vs.* $h\nu$ curves are also depicted in Fig. 3a (inset). The band gap value of the pristine BiOS was estimated to be 1.34 eV, consistent with previous studies. However, BiOS-OV possesses a smaller band gap value (1.28 eV) than the pristine BiOS. Fig. 3b shows the XPS valence spectra of BiOS and BiOS-OV, in which the valence band potentials (E_{VB}) of pristine BiOS and BiOS-OV are 1.01 and 0.92 eV, respectively. The conduction band potentials (E_{CB}) of BiOS and BiOS-OV were calculated to be approximately −0.33 and −0.36 eV, respectively. Their E_{CB} values were determined from Mott-Schottky plots. As depicted in Fig. S5, the patterns of BiOS and BiOS-OV exhibit positive slopes, indicating that both BiOS and BiOS-OV are n-type semiconductors. The flat-band potentials (E_{fb}) of BiOS and BiOS-OV were approximately −0.32 and −0.34 V *versus* Ag/AgCl, respectively. The E_{fb} values of BiOS and BiOS-OV were then calculated to be −0.12 and −0.14 V *versus* normal hydrogen electrode (NHE), respectively. The E_{CB} for the n-type semiconductor is more negative by approximately 0.2 V than its E_{fb} [36]. Therefore, the E_{CB} of pristine BiOS and BiOS-OV are −0.32 and −0.34 V *versus* NHE, in accordance with the above XPS valence spectra analyses.

DFT calculations were adopted to further reveal the electronic structure in the presence of rich oxygen va-

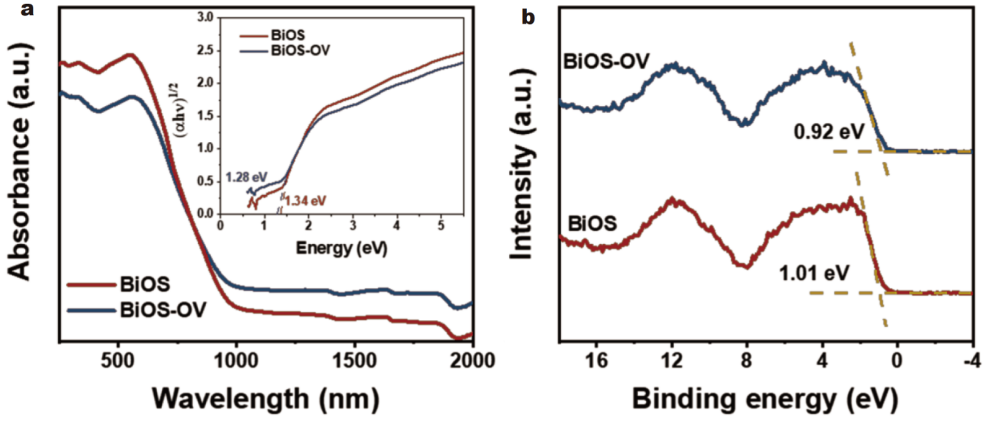

Figure 3 (a) UV-Vis-NIR DRS spectra of BiOS and BiOS-OV and their corresponding $(\alpha h\nu)^{1/2}$ *vs.* $h\nu$ curves (inset). (b) XPS valence spectra of BiOS and BiOS-OV.

cancies. The crystal structures of BiOS-OV and BiOS for the calculations are shown in Fig. 4a and b, respectively. Fig. 4c and d show the calculated density of states (DOS) of the BiOS-OV and BiOS. The rich oxygen vacancies introduce a new defect level, which results in a narrower band gap in BiOS-OV than in the pristine BiOS [29]. This result is in accordance with the experimental analyses. In addition, an increased DOS of defect level in BiOS-OV was observed compared with the pristine BiOS at the edge of the conduction band (CB), revealing that the electrons could easily transfer from the valence band (VB) to the CB in BiOS-OV. The newly formed defect level induced by oxygen vacancies could contribute to the photoexcitation of electrons to the CB and then transfer them from the CB to the surface defects. The electrostatic potentials of the BiOS-OV {−101} and BiOS {−101} surfaces are depicted in Fig. 4e and f, respectively. Evidently, the work function of BiOS is 5.14 eV, which is slightly larger than that of BiOS-OV (5.02 eV). The lower work function contributes to electron transfer and then helps to enhance the photocatalytic CO_2 reduction activity [37–39]. Based on the above results, the photocatalytic CO_2 reduction performance is facilitated by the changed electronic structure and lower work function after the introduction of rich oxygen vacancies.

The introduced rich oxygen vacancies in BiOS exhibit a meaningful effect on the separation efficiency of the photogenerated charge carriers, which is a vital factor for the photocatalytic CO_2 reduction reaction. Additionally, radiative recombination between the photogenerated carriers leads to PL emission. Generally, a lower PL peak intensity can be attributed to slower recombination of photogenerated charge carriers. As seen in Fig. 5a, BiOS-OV exhibits a lower PL peak intensity, indicating the slower recombination of generated charge carriers in BiOS-OV than in pristine BiOS. In addition, the abundant defects in BiOS-OV also lead to weaker PL emission. The recombination of electrons and holes are limited by abundant defects, and then more photogenerated electrons are transferred to participate in the photocatalytic CO_2 reduction process to boost the yield of CO_2 conversion to CH_4 [40]. Time-resolved fluorescence decay curves were used to further explore the charge transfer properties of the samples. The characteristic data are shown in Fig. 5b, and the average decay times of the photocatalysts were also calculated. Obviously, the average decay time of BiOS-OV (6.11 ns) is larger than that of pristine BiOS (4.11 ns), which is ascribed to the existence of rich oxygen vacancies serving as trapping sites to capture photoinduced electrons, suppressing the re-

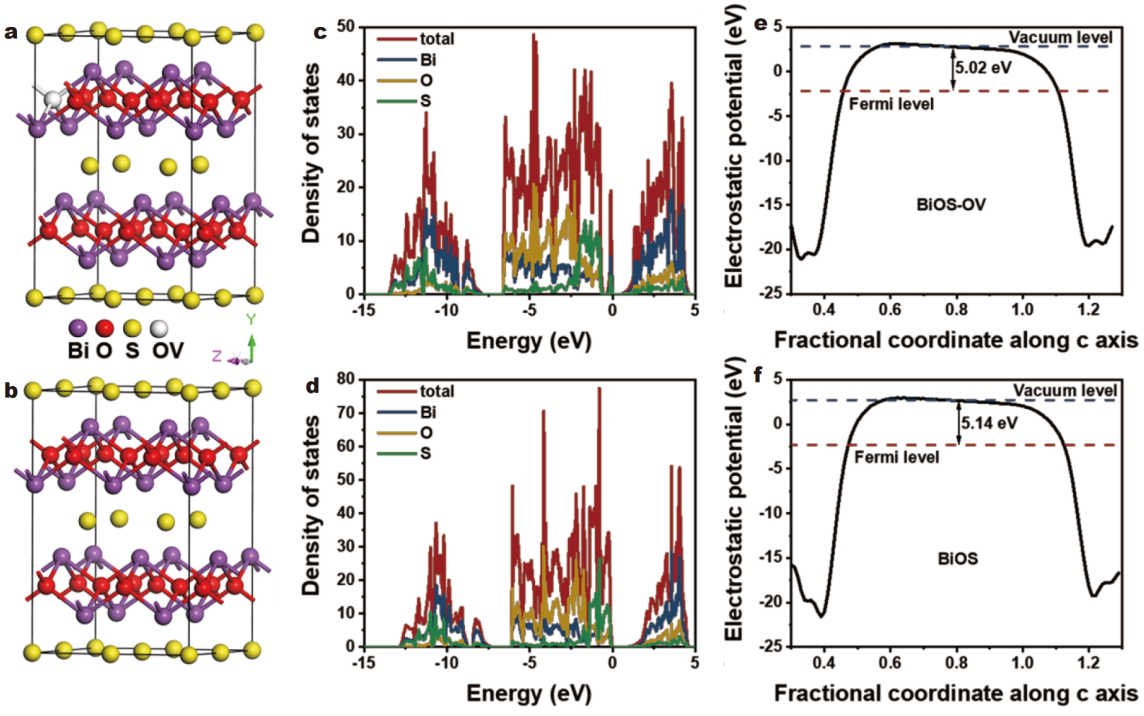

Figure 4 Schematic representation of the crystal structures of (a) BiOS-OV and (b) BiOS. The calculated DOS patterns of (c) BiOS-OV and (d) BiOS. The calculated work functions of (e) BiOS-OV and (f) BiOS.

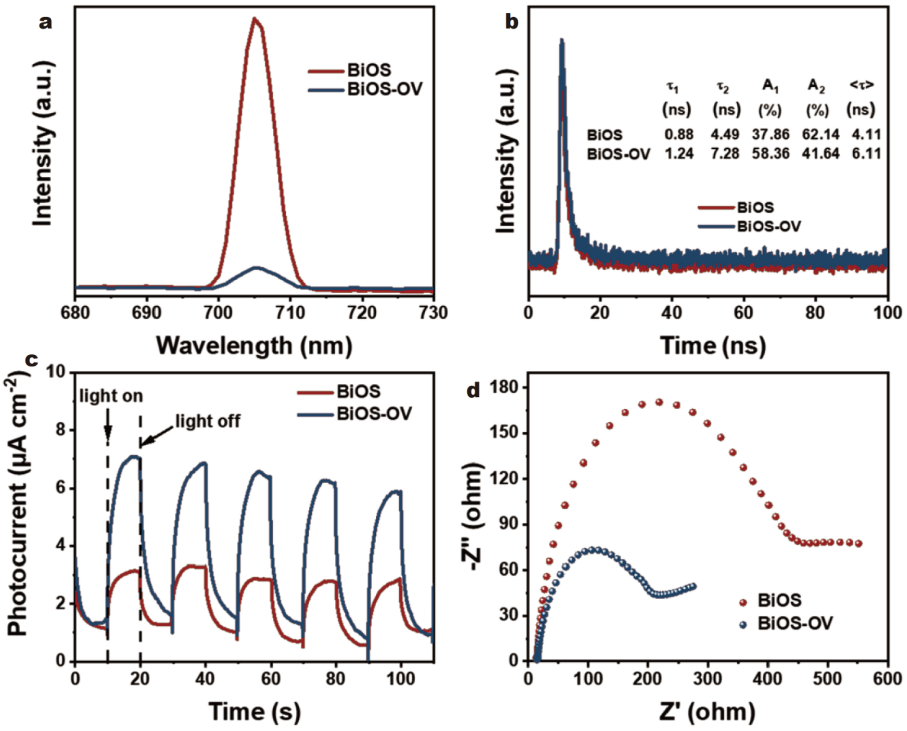

Figure 5 (a) PL spectra of BiOS and BiOS-OV. (b) Time-resolved fluorescence decay curves of BiOS and BiOS-OV. (c) Transient photocurrent responses and (d) EIS Nyquist impedance plots of BiOS and BiOS-OV.

combination of photogenerated carriers in BiOS-OV and thereby enhancing the efficiency of photocatalytic reactions [29]. The photocurrent is generated by the separation of photogenerated carriers. As shown in Fig. 5c, the photocurrent intensity in BiOS-OV is much higher (nearly 3-fold higher) than that in the pristine BiOS. This result further confirms that the photogenerated charge carriers could be efficiently separated in BiOS-OV because of the existence of rich oxygen vacancies. In addition, EIS Nyquist impedance plots of the as-prepared samples were obtained to explore the enhanced conductivity in BiOS-OV. As shown in Fig. 5d, smaller Nyquist plots were observed for BiOS-OV in contrast to the pristine BiOS, indicating that better charge transfer occurrs in BiOS-OV. Based on the above analyses, the separation and transfer efficiencies of the photoinduced electrons and holes are evidently facilitated in BiOS-OV, contributing to the photocatalytic CO_2 reduction.

The photocatalytic performances of the as-prepared samples were estimated by photocatalytic CO_2 reduction. Fig. 6a and b show the photocatalytic CO_2 performances of the BiOS samples with oxygen vacancies prepared under different heating conditions. Evidently, after the heating treatment, the photocatalytic CO_2 reduction performance of BiOS is highly enhanced, which could be ascribed to the effect of the oxygen vacancies generated by the thermal treatment. Among the samples, BiOS-OV prepared by heating treatment at 400°C for 4 h exhibits the highest CH_4 yield of 65.8 μmol g^{-1} for photocatalytic CO_2 reduction upon 90 min of visible light irradiation, which is almost 27-fold higher than that of the pristine BiOS (2.4 μmol g^{-1}), as shown in Fig. 6c. As the heating temperature and time further increased, the photocatalytic CO_2 reduction performance decreased, which could be ascribed to the massive amounts of vacancies acting as recombination centers for photogenerated carriers, resulting in a decrease in the photocatalytic CO_2 reduction performance [41]. Additionally, Fig. S6 shows the obvious O_2 signals after photocatalytic CO_2 reduction over BiOS-OV through oxidation of H_2O, revealing the completion of the photoredox cycle. The photocatalytic CO_2 reduction performances of the as-prepared samples under various conditions were also determined. As depicted in Fig. 6d, no obvious peak of CH_4 was observed in the GC spectra without the catalyst or with BiOS-OV in the absence of CO_2, indicating that photocatalytic CO_2

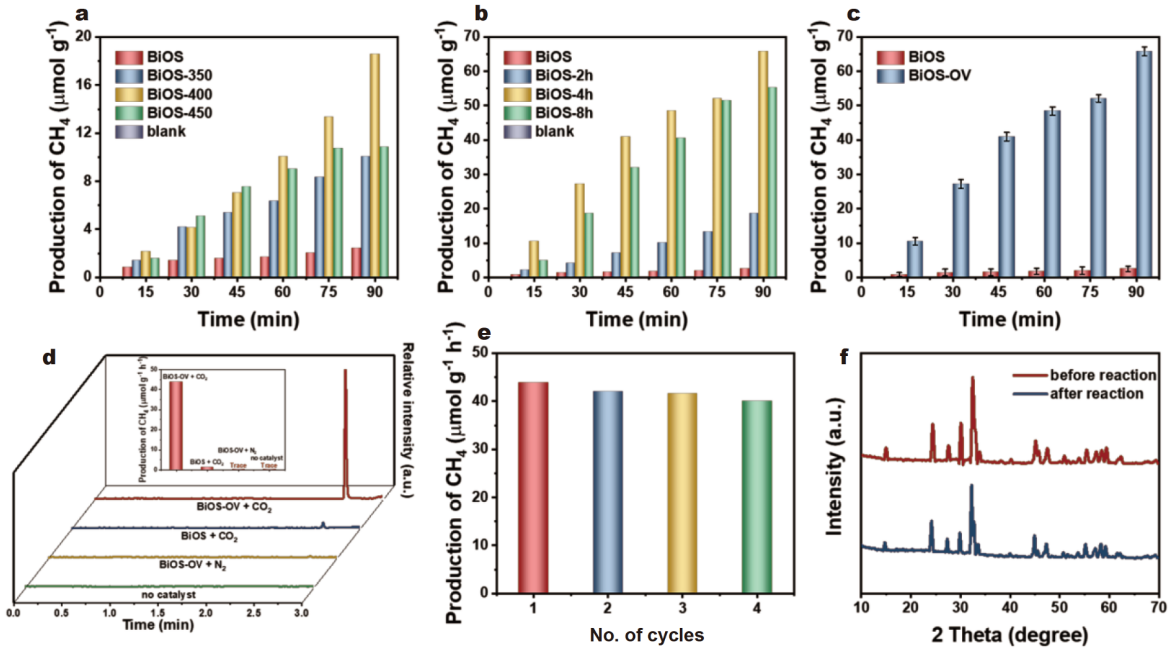

Figure 6 Photocatalytic CO_2 reduction performances of the pristine BiOS and BiOS with oxygen vacancies under visible light irradiation (λ > 420 nm): (a) different heating temperatures and (b) different heating times. (c) Photocatalytic CO_2 reduction performance comparison between pristine BiOS and BiOS-OV. (d) GC spectra of the photocatalytic CO_2 reduction reaction under various conditions (inset: corresponding CH_4 yields in the photocatalytic CO_2 reduction process). (e) Cycle experiments for photocatalytic CO_2 reduction over the BiOS-OV sample. (f) XRD patterns of the BiOS-OV samples before and after the photocatalytic CO_2 reduction reaction.

reduction requires photocatalysts and CO_2 and confirming the source of photocatalytic production. The figure inset shows the CH_4 yield for photocatalytic CO_2 reduction in detail. Cycle experiments of photocatalytic CO_2 reduction were performed to confirm the stability of BiOS-OV. As shown in Fig. 6e, the as-prepared BiOS-OV still shows excellent photocatalytic CO_2 reduction activity even after four cycles. Moreover, no obvious change was observed in the XRD patterns of the BiOS-OV samples before and after the reaction, as shown in Fig. 6f, further revealing the outstanding stability of BiOS-OV. Comparison studies of photocatalysts containing $[Bi_2O_2]^{2+}$ layers in previous studies were also performed. Table S2 shows that BiOS-OV exhibits the best photocatalytic activity and selectivity among these $[Bi_2O_2]^{2+}$-containing photocatalysts, indicating that BiOS-OV may be a promising and superb material for the photocatalytic reaction.

The existence of rich oxygen vacancies causes oxygen-deficient BiOS to be negatively charged compared with pristine BiOS, which contributes to the adsorption of CO_2 on the surface of BiOS-OV [29]. This was further confirmed through the CO_2 adsorption isotherms in Fig. 7a. Evidently, more CO_2 adsorption was observed in BiOS-OV than in pristine BiOS, revealing enhanced CO_2 adsorption and activation and thereby contributing to the redox reactions [37,42]. To further validate the enhanced chemisorption properties of CO_2 in BiOS-OV, CO_2-TPD profiles were obtained. According to previous studies, the temperature ranges between 50 and 150°C and between 150 and 250°C were assigned to the weak and medium adsorption for CO_2 from the CO_2-TPD profiles, respectively, while the higher temperature (above 250°C) corresponded to the stronger CO_2 adsorption [37]. As depicted in Fig. 7b, a peak at 518°C was observed in the profile of pristine BiOS, whereas a peak was observed at a higher temperature (539°C) in the profile of BiOS-OV. This result reveals that stronger CO_2 adsorption active sites are generated in BiOS-OV to boost the photocatalytic CO_2 reduction reaction [37,43]. DFT calculations were further adopted to confirm the experimental analyses. As shown in Fig. 7c–f, the introduced rich oxygen vacancies lead to different spatial distributions of the orbital wave function, and a more delocalized charge distribution was observed near the oxygen vacancies in BiOS-OV, which could be ascribed to the overlap of the

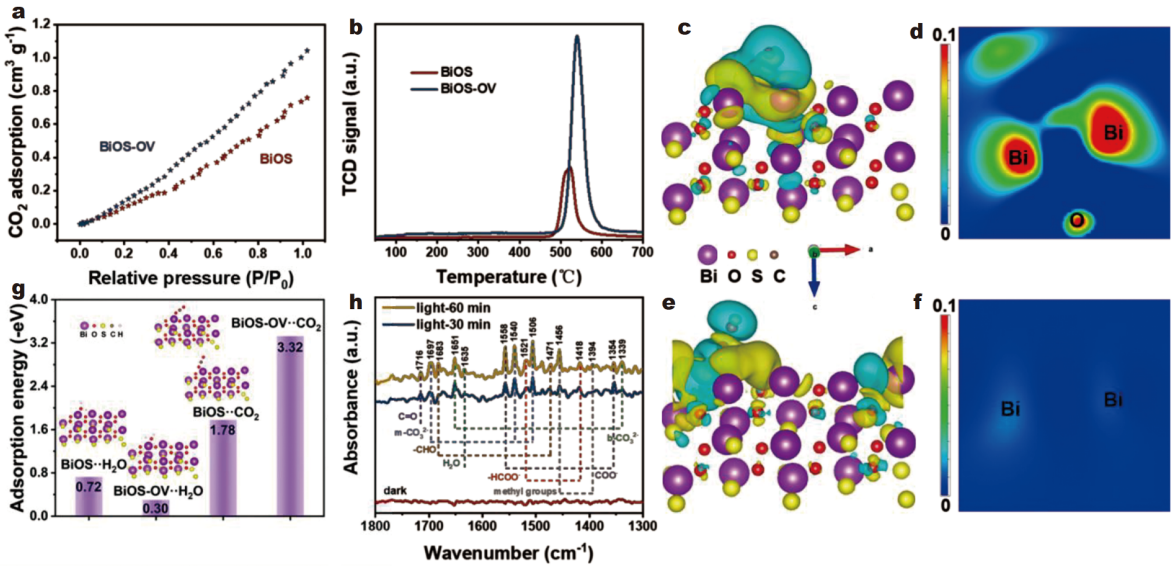

Figure 7 (a) CO_2 adsorption isotherms and (b) CO_2-TPD spectra of BiOS and BiOS-OV. The charge difference of CO_2 adsorbed in (c) BiOS-OV and (e) BiOS. Charge accumulation is shown in yellow, and the depletion is shown in light blue. Electronic localization function of (d) BiOS-OV and (f) BiOS. (g) The adsorption energies of H_2O and CO_2 adsorbed on BiOS and BiOS-OV samples (inset: the calculation models). (h) *In situ* FT-IR spectra of photocatalytic CO_2 reduction under visible light irradiation.

electronic orbitals on the Bi atom, thus favouring stabilization of the photocatalytic CO_2 reduction intermediates to decrease the energy barriers in this process [29]. Moreover, the adsorption energies of H_2O and CO_2 adsorbed on pristine BiOS and BiOS-OV were calculated. The structural models are shown in the inset in Fig. 7g. The adsorption energy of CO_2 adsorbed on BiOS-OV was calculated to be −3.32 eV, whereas an adsorption energy of −1.78 eV was obtained for CO_2 adsorbed on pristine BiOS, indicating the strong adsorption property of BiOS-OV for CO_2 in comparison with that of pristine BiOS. The theoretical calculation results were also in accordance with the experimental analyses. At the same time, the adsorption energy of H_2O adsorbed on BiOS-OV was calculated to be −0.30 eV, which exhibited a slightly weaker adsorption energy for H_2O in BiOS-OV in comparison with that of pristine BiOS (−0.72 eV). As studied in previous research, the stronger adsorption energy of CO_2 contributes to the stabilization of metal-CO_2 intermediates and hence enhances the photocatalytic CO_2 reduction performance, whereas the weaker adsorption energy of H_2O enables it to limit the generation of unexpected metal-H_2O adducts and thereby weakens the formation of H_2 [44]. Hence, the stronger CO_2 adsorption energy and the weaker H_2O adsorption energy favour the photocatalytic CO_2 reduction process simultaneously.

In situ FT-IR patterns were collected to further explore the photocatalytic CO_2 reduction process as exhibited in Fig. 7h. Before light irradiation, the spectrum was collected under a continuous mixture flow of ultrahigh CO_2 and H_2O for 30 min. Afterwards, light irradiation was introduced into the reaction system. Taking BiOS-OV as an example, it was clearly observed that the peaks were more apparent with increasing light irradiation from 0 to 60 min. The peaks at 1506, 1540 and 1697 cm^{-1} matched well with monodentate carbonate (m-CO_3^{2-}) and the peaks located at 1339 and 1651 cm^{-1} were assigned to bidentate carbonate (b-CO_3^{2-}), confirming the presence of adsorbed CO_2 [45–49]. As the light irradiation increased, the intensities of the typical peaks showed an obvious increase. In particular, the peaks at 1354 and 1558 cm^{-1} matched well with COO^-, whereas the peaks centered at 1418 and 1521 cm^{-1} could be assigned to –$HCOO^-$. The strengthened intensities of bidentate formate species (COO^- and –$HCOO^-$) revealed that HCOOH could act as a vital intermediate in photocatalytic CO_2 reduction over BiOS-OV [50]. Additionally, the appearance of the peak at 1716 cm^{-1} matched well with C=O, and its intensity increased with increasing irradiation time, revealing that trace CO might be formed during this photocatalytic process. This result indicated that the formate multi-electron pathway might occur during the photocatalytic CO_2 reduction process, in which 2, 4, 6 and 8 electrons were required for the for-

mation of HCOOH, HCHO, CH_3OH and CH_4 [51]. Hence, it was suggested that the formed CO from formate species acted as the intermediate for photocatalytic CO_2 reduction to CH_4 [52,53]. Furthermore, the presence of methyl groups (1394 and 1456 cm^{-1}) further revealed the formation of CH_4 [54,55]. Based on the above analyses, it is possible that the reduction of formate species to CH_4 occurred over BiOS-OV because more electrons with longer lifetimes were observed in BiOS-OV.

CONCLUSIONS

The $[Bi_2O_2]^{2+}$-containing material BiOS with rich oxygen vacancies was successfully prepared through thermal treatment at various heating temperatures and times. The as-obtained photocatalysts were employed to catalyze CO_2 photoconversion. BiOS-OV exhibited the best photocatalytic CO_2 reduction activity with a CH_4 yield of 65.8 μmol g^{-1} under visible light irradiation within 90 min, which is almost 27-fold higher than that of pristine BiOS. The outstanding photocatalytic activity of BiOS-OV was ascribed to the existence of rich oxygen vacancies, leading to abundant active sites and excellent CO_2 adsorption according to the theoretical and experimental results. Moreover, BiOS-OV suppressed the recombination of photogenerated carriers and facilitated efficient separation. The existence of rich oxygen vacancies in BiOS-OV also contributed to the activation of CO_2. The theoretical calculation and experimental analyses demonstrate the vital effect of rich oxygen vacancies on the photocatalytic CO_2 reduction process. Engineering the electronic structure of BiOS through the introduction of rich oxygen vacancies could be a robust approach to enhance the photocatalytic performance of BiOS. This work is expected to be favorable for constructing $[Bi_2O_2]^{2+}$-containing photocatalysts with highly efficient photocatalytic performance through vacancy engineering.

Received 12 November 2020; accepted 21 January 2021; published online 9 April 2021

1 Liu L, Huang H, Chen F, *et al.* Cooperation of oxygen vacancies and 2D ultrathin structure promoting CO_2 photoreduction performance of $Bi_4Ti_3O_{12}$. Sci Bull, 2020, 65: 934–943
2 Li J, Huang B, Guo Q, *et al.* Van der Waals heterojunction for selective visible-light-driven photocatalytic CO_2 reduction. Appl Catal B-Environ, 2021, 284: 119733
3 Yi L, Zhao W, Huang Y, *et al.* Tungsten bronze $Cs_{0.33}WO_3$ nanorods modified by molybdenum for improved photocatalytic CO_2 reduction directly from air. Sci China Mater, 2020, 63: 2206–2214
4 Jiang L, Wang K, Wu X, *et al.* Highly enhanced full solar spectrum-driven photocatalytic CO_2 reduction performance in $Cu_{2-x}S$/g-C_3N_4 composite: Efficient charge transfer and mechanism insight. Sol RRL, 2021, 5: 2000326
5 Li M, Li D, Zhou Z, *et al.* Plasmonic Ag as electron-transfer mediators in Bi_2MoO_6/Ag-AgCl for efficient photocatalytic inactivation of bacteria. Chem Eng J, 2020, 382: 122762
6 Zhong Q, Li Y, Zhang G. Two-dimensional MXene-based and MXene-derived photocatalysts: Recent developments and perspectives. Chem Eng J, 2021, 409: 128099
7 Wang L, Lv D, Yue Z, *et al.* Promoting photoreduction properties *via* synergetic utilization between plasmonic effect and highly active facet of BiOCl. Nano Energy, 2019, 57: 398–404
8 Li J, Dong X, Zhang G, *et al.* Probing ring-opening pathways for efficient photocatalytic toluene decomposition. J Mater Chem A, 2019, 7: 3366–3374
9 Li H, Shang H, Cao X, *et al.* Oxygen vacancies mediated complete visible light NO oxidation *via* side-on bridging superoxide radicals. Environ Sci Technol, 2018, 52: 8659–8665
10 Li M, Yu S, Huang H, *et al.* Unprecedented eighteen-faceted BiOCl with a ternary facet junction boosting cascade charge flow and photo-redox. Angew Chem Int Ed, 2019, 58: 9517–9521
11 Wang Y, Wang K, Wang J, *et al.* Sb_2WO_6/BiOBr 2D nanocomposite S-scheme photocatalyst for NO removal. J Mater Sci Tech, 2020, 56: 236–243
12 Cui D, Wang L, Xu K, *et al.* Band-gap engineering of BiOCl with oxygen vacancies for efficient photooxidation properties under visible-light irradiation. J Mater Chem A, 2018, 6: 2193–2199
13 Ma Z, Li P, Ye L, *et al.* Oxygen vacancies induced exciton dissociation of flexible BiOCl nanosheets for effective photocatalytic CO_2 conversion. J Mater Chem A, 2017, 5: 24995–25004
14 Wang H, Yong D, Chen S, *et al.* Oxygen-vacancy-mediated exciton dissociation in BiOBr for boosting charge-carrier-involved molecular oxygen activation. J Am Chem Soc, 2018, 140: 1760–1766
15 Bai J, Sun J, Zhu X, *et al.* Enhancement of solar-driven photocatalytic activity of BiOI nanosheets through predominant exposed high energy facets and vacancy engineering. Small, 2020, 16: 1904783
16 Koyama E, Nakai I, Nagashima K. Crystal chemistry of oxide–chalcogenides. II. Synthesis and crystal structure of the first bismuth oxide–sulfide, Bi_2O_2S. Acta Crystlogr B Struct Sci, 1984, 40: 105–109
17 Zhang X, Liu Y, Zhang G, *et al.* Thermal decomposition of bismuth oxysulfide from photoelectric Bi_2O_2S to superconducting $Bi_4O_4S_3$. ACS Appl Mater Interfaces, 2015, 7: 4442–4448
18 Wu Z, Yu H, Shi S, *et al.* Bismuth oxysulfide modified ZnO nanorod arrays as an efficient electron transport layer for inverted polymer solar cells. J Mater Chem A, 2019, 7: 14776–14789
19 Huang C, Yu H, Chen J, *et al.* Improved performance of polymer solar cells by doping with Bi_2O_2S nanocrystals. Sol Energy Mater Sol Cells, 2019, 200: 110030
20 Chen J, Bi Z, Xu X, *et al.* The low temperature solution-processable SnO_2 modified by Bi_2O_2S as an efficient electron transport layer for perovskite solar cells. Electrochim Acta, 2020, 330: 135197
21 Pacquette AL, Hagiwara H, Ishihara T, *et al.* Fabrication of an oxysulfide of bismuth Bi_2O_2S and its photocatalytic activity in a Bi_2O_2S/In_2O_3 composite. J PhotoChem PhotoBiol A-Chem, 2014, 277: 27–36
22 Xing Z, Hu J, Ma M, *et al.* From one to two: *In situ* construction of an ultrathin 2D-2D closely bonded heterojunction from a single-phase monolayer nanosheet. J Am Chem Soc, 2019, 141: 19715–19727
23 Bai F, Xu L, Zhai X, *et al.* Vacancy in ultrathin 2D nanomaterials toward sustainable energy application. Adv Energy Mater, 2020,

10: 1902107
24 Cheng Q, Zhang GK. Enhanced photocatalytic performance of tungsten-based photocatalysts for degradation of volatile organic compounds: a review. Tungsten, 2020, 2: 240–250
25 Wang Z, Jiang L, Wang K, *et al.* Novel AgI/$BiSbO_4$ heterojunction for efficient photocatalytic degradation of organic pollutants under visible light: Interfacial electron transfer pathway, DFT calculation and degradation mechanism study. J Hazard Mater, 2020, doi: 10.1016/j.jhazmat.2020.124948
26 Wang K, Jiang L, Wu X, *et al.* Vacancy mediated Z-scheme charge transfer in a 2D/2D $La_2Ti_2O_7$/g-C_3N_4 nanojunction as a bifunctional photocatalyst for solar-to-energy conversion. J Mater Chem A, 2020, 8: 13241–13247
27 Jiang L, Wang K, Wu X, *et al.* Amorphous bimetallic cobalt nickel sulfide cocatalysts for significantly boosting photocatalytic hydrogen evolution performance of graphitic carbon nitride: efficient interfacial charge transfer. ACS Appl Mater Interfaces, 2019, 11: 26898–26908
28 Wang S, Hai X, Ding X, *et al.* Light-switchable oxygen vacancies in ultrafine Bi_5O_7Br nanotubes for boosting solar-driven nitrogen fixation in pure water. Adv Mater, 2017, 29: 1701774
29 Wu J, Li X, Shi W, *et al.* Efficient visible-light-driven CO_2 reduction mediated by defect-engineered biobr atomic layers. Angew Chem Int Ed, 2018, 57: 8719–8723
30 Lei F, Sun Y, Liu K, *et al.* Oxygen vacancies confined in ultrathin indium oxide porous sheets for promoted visible-light water splitting. J Am Chem Soc, 2014, 136: 6826–6829
31 Li H, Qin F, Yang Z, *et al.* New reaction pathway induced by plasmon for selective benzyl alcohol oxidation on BiOCl possessing oxygen vacancies. J Am Chem Soc, 2017, 139: 3513–3521
32 Li Z, Yan Q, Jiang Q, *et al.* Oxygen vacancy mediated $Cu_yCo_{3-y}Fe_1O_x$ mixed oxide as highly active and stable toluene oxidation catalyst by multiple phase interfaces formation and metal doping effect. Appl Catal B-Environ, 2020, 269: 118827
33 Yang G, Miao W, Yuan Z, *et al.* Bi quantum dots obtained *via in situ* photodeposition method as a new photocatalytic CO_2 reduction cocatalyst instead of noble metals: Borrowing redox conversion between Bi_2O_3 and Bi. Appl Catal B-Environ, 2018, 237: 302–308
34 Gao X, Gao K, Fu F, *et al.* Synergistic introducing of oxygen vacancies and hybrid of organic semiconductor: realizing deep structure modulation on Bi_5O_7I for high-efficiency photocatalytic pollutant oxidation. Appl Catal B-Environ, 2020, 265: 118562
35 Zhao K, Zhang Z, Feng Y, *et al.* Surface oxygen vacancy modified Bi_2MoO_6/MIL-88B(Fe) heterostructure with enhanced spatial charge separation at the bulk & interface. Appl Catal B-Environ, 2020, 268: 118740
36 Hao X, Zhou J, Cui Z, *et al.* Zn-vacancy mediated electron-hole separation in ZnS/g-C_3N_4 heterojunction for efficient visible-light photocatalytic hydrogen production. Appl Catal B-Environ, 2018, 229: 41–51
37 Zhang A, He R, Li H, *et al.* Nickel doping in atomically thin tin disulfide nanosheets enables highly efficient CO_2 reduction. Angew Chem Int Ed, 2018, 57: 10954–10958
38 Tarasov A, Zhang S, Tsai MY, *et al.* Controlled doping of large-area trilayer MoS_2 with molecular reductants and oxidants. Adv Mater, 2015, 27: 1175–1181
39 Miao P, Zhang Z, Sun J, *et al.* Orbital angular momentum microlaser. Science, 2016, 353: 464–467
40 Tan L, Xu SM, Wang Z, *et al.* Highly selective photoreduction of CO_2 with sppressing H_2 evolution over monolayer layered double hydroxide under irradiation above 600 nm. Angew Chem Int Ed, 2019, 58: 11860–11867
41 Song X, Li X, Zhang X, *et al.* Fabricating C and O co-doped carbon nitride with intramolecular donor-acceptor systems for efficient photoreduction of CO_2 to CO. Appl Catal B-Environ, 2020, 268: 118736
42 Liang HP, Acharjya A, Anito DA, *et al.* Rhenium-metalated polypyridine-based porous polycarbazoles for visible-light CO_2 photoreduction. ACS Catal, 2019, 9: 3959–3968
43 Cui X, Gao P, Li S, *et al.* Selective production of aromatics directly from carbon dioxide hydrogenation. ACS Catal, 2019, 9: 3866–3876
44 Wang Y, Huang NY, Shen JQ, *et al.* Hydroxide ligands cooperate with catalytic centers in metal–organic frameworks for efficient photocatalytic CO_2 reduction. J Am Chem Soc, 2018, 140: 38–41
45 Di T, Zhu B, Cheng B, *et al.* A direct Z-scheme g-C_3N_4/SnS_2 photocatalyst with superior visible-light CO_2 reduction performance. J Catal, 2017, 352: 532–541
46 Xu D, Cheng B, Wang W, *et al.* Ag_2CrO_4/g-C_3N_4/graphene oxide ternary nanocomposite Z-scheme photocatalyst with enhanced CO_2 reduction activity. Appl Catal B-Environ, 2018, 231: 368–380
47 Tasbihi M, Fresno F, Simon U, *et al.* On the selectivity of CO_2 photoreduction towards CH_4 using Pt/TiO_2 catalysts supported on mesoporous silica. Appl Catal B-Environ, 2018, 239: 68–76
48 Yang X, Wang S, Yang N, *et al.* Oxygen vacancies induced special CO_2 adsorption modes on Bi_2MoO_6 for highly selective conversion to CH_4. Appl Catal B-Environ, 2019, 259: 118088
49 Fu J, Bao H, Liu Y, *et al.* CO_2 reduction: Oxygen doping induced by nitrogen vacancies in Nb_4N_5 enables highly selective CO_2 reduction. Small, 2020, 16: 2070007
50 Jiang Z, Sun H, Wang T, *et al.* Nature-based catalyst for visible-light-driven photocatalytic CO_2 reduction. Energy Environ Sci, 2018, 11: 2382–2389
51 Habisreutinger SN, Schmidt-Mende L, Stolarczyk JK. Photocatalytic reduction of CO_2 on TiO_2 and other semiconductors. Angew Chem Int Ed, 2013, 52: 7372–7408
52 Wang K, Fu J, Zheng Y. Insights into photocatalytic CO_2 reduction on C_3N_4: Strategy of simultaneous B, K co-doping and enhancement by N vacancies. Appl Catal B-Environ, 2019, 254: 270–282
53 Tan SS, Zou L, Hu E. Kinetic modelling for photosynthesis of hydrogen and methane through catalytic reduction of carbon dioxide with water vapour. Catal Today, 2008, 131: 125–129
54 Sun Z, Fischer JMTA, Li Q, *et al.* Enhanced CO_2 photocatalytic reduction on alkali-decorated graphitic carbon nitride. Appl Catal B-Environ, 2017, 216: 146–155
55 Li W, Zhang G, Jiang X, *et al.* CO_2 hydrogenation on unpromoted and M-promoted Co/TiO_2 catalysts (M = Zr, K, Cs): Effects of crystal phase of supports and metal–support interaction on tuning product distribution. ACS Catal, 2019, 9: 2739–2751

Acknowledgements This work was supported by the Science and Technology Planning Project of Shenzhen Municipality (JCYJ20200109150225155), the Natural Science Foundation of Hubei Province (2016CFA078), the National Natural Science Foundation of China (51472194 and 21975193) and the Fundamental Research Funds for the Central Universities (2020-YB-031).

Author contributions Jiang L conceived the experiments and wrote the original draft under the supervision of Zhang G; Li Y worked on the

formal analysis; Wu X provided the experimental resources and suggestions for this experiment; Zhang G proposed the concept of this work, provided suggestions for the experiments and edited the manuscript. All authors contributed to the general discussion.

Conflict of interest The authors declare that they have no conflict of interest.

Supplementary information Supporting data are available in the online version of the paper.

Lisha Jiang is currently a PhD candidate at the School of Resources and Environmental Engineering, Wuhan University of Technology. She obtained her BSc degree from Wuhan University of Technology in 2016. Her PhD research focuses on the design of novel photocatalysts for solar-to-energy conversion.

Gaoke Zhang is a full professor at the School of Resources and Environmental Engineering, Wuhan University of Technology. From 2005 to 2006, he was an adjunct professor at Materials Research Institute, Pennsylvania State University. His research interests focus on nanomaterials, novel photocatalysts, advanced oxidation process and adsorption materials for environmental and energy applications.

富氧空位修饰的铋氧硫晶体用于光催化二氧化碳还原转化为甲烷

姜丽莎[1], 李源[1], 吴晓勇[1], 张高科[1,2,3*]

摘要 制备高效光催化剂将二氧化碳还原转化为有价值的化学品, 是缓解能源危机和环境污染的有效措施. 本论文通过高温焙烧法, 制备了富氧空位修饰的Bi_2O_2S光催化剂, 并将其用于可见光驱动的CO_2光还原, 确定了富氧空位修饰的Bi_2O_2S光催化剂的最佳制备条件. 通过一系列实验及表征, 证实了BiOS-OV中丰富氧空位的存在; 结合理论计算深入分析了引入的丰富氧空位对Bi_2O_2S光催化剂的内部电子结构及光化学性能等的影响. 深入研究了整个体系中光催化CO_2还原反应的具体步骤, 旨在揭示丰富氧空位的存在引起CO_2光还原性能提高的根本原因.

